Research Article

Maryamsadat Shahidi[#], Omid Abazari[#], Parisa Dayati, Ali Bakhshi, Azam Rasti, Fateme Haghiralsadat, Seyed Morteza Naghib*, and Davood Tofighi

Aptamer-functionalized chitosan-coated gold nanoparticle complex as a suitable targeted drug carrier for improved breast cancer treatment

https://doi.org/10.1515/ntrev-2022-0479
received April 20, 2022; accepted August 16, 2022

Abstract: In the following research, we specifically assessed the feasibility of a novel AS-1411-chitosan (CS)-gold nanoparticle (AuNPs) delivery system to carry methotrexate (MTX) into the cancer cells. The designed system had a spherical shape with average size of 62 ± 2.4 nm, the zeta potential of −32.1 ± 1.4 mV, and released MTX in a controlled pH- and time-dependent manner. CS-AuNPs could successfully penetrate the breast cancer cells and release the therapeutic drug, and ultimately, be accumulated by the nucleolin-AS1411 targeting mechanism within the *in vivo* environment. The anticancer activity of MTX was attributed to the induction of mitochondria membrane potential loss and nuclear fragmentation, which leads to apoptotic death. Moreover, the cellular internalization confirmed the high potential in the elimination of cancer cells without notable cytotoxicity on non-target cells. Therefore, it was concluded that the AS1411-CS-AuNPs with considerable *in vitro* and *in vivo* results could be utilized as a favorable system for breast cancer treatment.

Keywords: methotrexate, chitosan, gold, aptamer, breast cancer, nanoparticle, delivery system

1 Introduction

The latest global cancer statistics elucidated that 2.3 million new cancer cases and 685,000 deaths occurred due to breast cancer in 2020 [1]. Over the past decades, different procedures have been licensed in the context of cancer therapy and led to a higher survival rate [2]. Among all commonly used procedures, chemotherapy still remained the mainstream strategy to treat an extended range of cancers in clinical practice; nonetheless, its efficiency is strictly reduced because of the systemic drug distribution and low therapeutic indices of chemotherapeutic drugs [3]. It seems, drug delivery nanosystems are promising for cancer therapy [4–8].

Methotrexate (MTX) is a folic acid antagonist approved for treating and managing rheumatoid arthritis. Moreover, a recent investigation displayed the high capability of MTX as an agent to combat a variety of human cancer types like ovarian and breast cancers [9,10]. MTX can bind to folate receptors, impair DNA synthesis, and induce cell death in the rapid proliferation of breast cancer cells [11]. Despite the extensive clinical application of MTX, its efficacy is restricted due to the poor water solubility, short half-life, and severe toxic effects on healthy tissues [12].

Gold nanoparticles (AuNPs) are a favorable nanomaterial in numerous medical applications, especially in controlled drug delivery and medical imaging, owing to their strong photostability, ease of synthesis, chemical stability, and low toxicity [13]. However, the full potential of these NPs is limited in living systems because of the direct interaction between the NPs and blood proteins,

# These authors contributed equally to this work and should be considered first co-authors.

*** Corresponding author: Seyed Morteza Naghib,** Nanotechnology Department, School of Advanced Technologies, Iran University of Science and Technology, Tehran, Iran, e-mail: naghib@iust.ac.ir
Maryamsadat Shahidi, Omid Abazari, Ali Bakhshi: Department of Clinical Biochemistry, School of Medicine, Shahid Sadoughi University of Medical Sciences and Health Services, Yazd, Iran
Parisa Dayati: Department of Clinical Biochemistry, Faculty of Medical Sciences, Tarbiat Modares University, Tehran, Iran
Azam Rasti: Department of Medical Genetics, School of Medicine, Tehran University of Medical Sciences, Tehran, Iran
Fateme Haghiralsadat: Department of Advanced Medical Sciences and Technologies, School of Paramedicine, Shahid Sadoughi University of Medical Sciences, Yazd, Iran
Davood Tofighi: Department of Psychology, Epidemiology, and Research Design Support (BERD), Clinical and Translational Science Center, University of New Mexico, Mexico, Albuquerque, New Mexico, United States of America

which affects the biological behavior and functionality of the NPs, resulting in inflammatory responses and insufficient delivery to target cells [14].

Chitosan (CS)-coated nanocarriers have a remarkable potential to be placed in biomedical applications [15–17]. CS is a natural polymer procured from chitin deacetylation, and its unique characteristics, such as non-toxicity, low immunogenicity, biodegradability, and biocompatibility, made it an attractive choice for delivery systems [18]. Additionally, it is documented that CS as a cationic polymer gives a positive charge to the surface of nanocarriers and enhances their affinity to contact negatively charged targets such as nucleic acids and cell membranes [19]. Site-specific drug delivery can be improved by decorating CS with specific ligands that couple to targets overexpressed on cancerous cells' surfaces [20].

Aptamers are molecular recognition elements that include peptides and nucleic acids (RNA and ssDNA) that bind to a specific target molecule [21,22]. It is noteworthy that the AS1411, as one particular guanine-rich DNA aptamer, can attach to nucleolin as its target protein. Also, its expression on the surface of several cancer cells, like breast cancer, is highly observed but absent on normal cells [23].

In this research, we designed the AS1411-decorated CS-AuNPs complex not only to conquer the negative limitation of MTX but also to enhance the delivery mechanism by modifying the surface of AuNPs with biocompatible and biodegradable CS [24,25]. For this purpose, AuNPs are first conjugated by CS and then loaded with aptamer and MTX. To acquire the desired therapeutic consequence, the formulation containing MTX was optimized in particle size, zeta potential (ZP), and MTX loading. The resulted complex was examined in both *in vitro* and *in vivo* conditions to evaluate the delivery and impact of MTX on the proliferation of breast cancer. Moreover, to explore the specific effects of the complex on cancer cells, cultured Chinese hamster ovary (CHO) cells were employed as the control group.

2 Materials and methods

2.1 Materials and reagents

For this experiment, trypsin-ethylenediaminetetraacetic acid (EDTA), fetal bovine serum (FBS), DAPI (D8417), ethidium bromide, penicillin–streptomycin, Dulbecco's modified Eagle medium (DMEM, Gibco, Massachusetts, USA), 50–190 kDa CS (deacetylation degree = 85%), 1-ethyl-3-(3-dimethyl aminopropyl) carbodiimide hydrochloride (EDC), gold(III) chloride trihydrate ($HAuCl_4{\cdot}3H_2O$), 3-(4,5-dimethylthiazol-2-yl)-2,5-diphenyltetrazolium bromide (MTT), and MTX (Sigma-Aldrich, Missouri, USA) were acquired. The AS1411 aptamer with the sequence of 5′-GGTGGTGGTGGTTGT GGTGGTGGTGG-3′ was supplied from Yahooteb Novin Co.

2.2 Cell culture

The cell lines of MDA-MB-231, MCF-7 (as the target groups), and CHO (as the control group) were acquired from Tehran's Pasteur Institute of Iran. All cell lines were individually cultured in 4.5 g/L glucose DMEM enriched by 1% antibiotic and 10% FBS, then incubated in a humidified atmosphere with 37°C and 5% CO_2. Each cell line was checked daily under a microscope to observe confluency, and the culture mediums were renewed every 3 days.

2.3 Preparation of CS-AuNPs

In the beginning, the synthesis of AuNPs was performed according to Turkevich *et al.*'s previously described report. In brief, 20 mL of 1 mM $HAuCl_4{\cdot}3H_2O$ was added to a 50 mL Erlenmeyer flask and boiled under vigorous stirring. Afterward, 2 mL of trisodium citrate solution (1%) and a reducing agent were quickly loaded into the boiling solution and continued stirring for 15 min. Next the heater was turned off, and the solution was stirred for an additional 15 min. At the end of the reaction, the color of the mixture turned from light yellow to deep red, representing the formation of AuNPs. Centrifugation at 12,000 rpm for 20 min was performed to discard the large particles. Ultimately, the obtained supernatant was dialyzed and freeze-dried, respectively.

In the next step, CS (20 mg) and acetic acid (1 mL, 1% v/v) solution were mixed and stirred for 24 h. Next 1,000 µL of AuNPs solution (pH 6.0) was added to 40 µL of the prepared CS solution under magnetic stirring for 2 h [26]. The resultant mixture was stored at 4°C for further studies.

In the final step, to synthesize Apt-CS-AuNPs conjugate, 1,000 µL of the CS-AuNPs solution and 10 µL of AS1411 (100 µM, activated with EDC/NHS) were mixed (pH 7.4) and kept for 1.5 h at room temperature. The obtained Apt-CS-AuNP was centrifuged at 20,000 rpm for 20 min to remove non-reactive AS1411. After centrifugation, the resulted Apt-CS-AuNP was dissolved in PBS and kept at –20°C.

Meanwhile, 8 mg EDC, 5 mg MTX, and 5 mg NHS were dispersed in 5 mL of PBS (pH 7.4) and kept in an incubator

for 0.5 h at room temperature. To load MTX on the prepared Apt-CS-AuNPs, both suspensions were mixed and stirred for 48 h. The resulted MTX-Apt-CS-AuNP bioconjugate was centrifuged at 20,000 rpm for 0.5 h and lyophilized for 24 h. The presence of MTX in this bioconjugate was verified by using an ultraviolet-visible (UV-vis) spectroscopy at 306 nm. The supernatant was collected for further indirect calculation of the drug-loading content. A dynamic light scattering (DLS) with a Zetasizer analyzer (Nano-Z, Malvern, UK) was employed to assess the surface potential of the NPs at 25°C. Fourier transform infrared spectroscopy (FTIR, Thermo Fisher Scientific, USA) was performed to distinguish the functional groups of NPs using KBr pellets at 4 cm^{-1} resolution from 4,000 to 400 cm^{-1}. The DLS measurements were conducted at pH 7.4 and 5.5 at room temperature [27]. Transmission electron microscopy (TEM, HT7700, Tokyo, Japan, Hitachi) was implemented to determine the average size of NPs. Also, the absorption of AS1411 molecules on the CS-AuNPs surface was evaluated by measuring the absorbance of AS1411-CS-AuNPs conjugate at 260 nm by a UV spectrophotometer (Cambridge, UK).

2.4 *In vitro* drug-release study

To evaluate the performance of the MTX-AS1411-CS-AuNPs complex on the pH-dependent release of MTX, the complex was dispersed in 30 mL of PBS buffer at 5.5 and 7.4 pH in a dialysis bag (molecular cut-off, 2.0 kDa) under gentle stirring at 37°C. At certain time intervals (0–72 h), the release media (3 mL) was taken out and replaced with an equal volume of fresh buffer. The percentage of released MTX in certain time points was investigated by UV-vis absorbance at 306 nm. The cumulative release percentage of MTX was measured employing a standard curve.

2.5 *In vitro* stability of NPs

To monitor the *in vitro* stability of AuNPs and MTX-Apt-AuNPs-CS complex, the freeze-dried AuNPs and MTX-Apt-AuNPs-CS complex was re-suspended in PBS buffer (1:10 volume ratio). Then, the ZP and average size were measured regularly by DLS for 1 week.

2.6 Agarose gel electrophoresis

For evaluating AS1411 loading confirmation, the AS1411 molecules were mixed with the CS-AuNPs complex in a total volume of 10 µL in PBS or FBS at pH 7.5. The mobility of free AS1411 (positive control) and Apt-AuNPs-CS conjugate were evaluated by 2% (w/v) agarose gel electrophoresis containing ethidium bromide (1 h, 60 V).

2.7 AS1411 conjugation efficiency

To investigate the AS1411 conjugation efficiency, the AS1411 molecules were mixed with the CS-AuNPs complex and incubated for 24 h in the dialysis cassette. The unbounded AS1411 molecules were deleted from the AS1411-CS-AuNPs suspension using a dialysis cassette (3.5 kDa) during 48 h incubation. The AS1411-CS-AuNPs conjugate will be trapped in the cassette during the dialysis procedure, and the unconjugated AS1411 molecules will move from the cassette into the surrounding solution. The amount of unbounded AS1411 molecules was indirectly quantified by measuring its absorption at 260 nm and the AS1411 standard curve [28].

$$\text{Efficiency\%} = \frac{\text{The total amount of AS1411 added} - \text{Unbounded AS1411}}{\text{The total amount of AS1411 added}} \times 100.$$

2.8 Cellular uptake using fluorescence microscopy

To explore the MTX-Apt-AuNPs-CS complex's cellular internalization, the target cells were cultured at 10^5 cells/well on confocal plates (35 mm) at 37°C for 0.5 days. The culture media was swapped with 2 mL of serum-free medium containing desired formulations and incubated for 4 h to investigate the uptake. Next the fluorescence images were obtained at the excitation of 559 nm and 400× magnification.

2.9 Cell toxicity assessment

The *in vitro* cytotoxicity of Apt-AuNPs-CS (without MTX), free MTX, MTX-AuNPs-CS (without Apt), and MTX-Apt-AuNPs-CS against all cell lines were measured at certain time points using an MTT cell viability kit according to manufacturer's instructions. In brief, a density of 6×10^3 cells/well was planted in a 35 mm culture dish and incubated overnight. Cell in the logarithmic phase was utilized for treatment with concentrations of 0, 10, 25, 50,

100, 200, 300, and 500 μg/mL of each drug formulation for 24 h. After incubation for 4 h, MTT (20 μL, 5 mg/mL in PBS) was transferred to each well. Ultimately, the formed crystals were dissolved in dimethyl sulfoxide (DMSO, 200 μL) and read by a microplate reader (BioTek, USA) at 570 nm.

2.10 Morphological modifications of cell nuclei

The target cells were cultured at 2×10^4 concentrations in a 35 mm culture plate and maintained overnight. The breast cancer cells were incubated with free MTX and MTX-Apt-AuNPs-CS at a 100 μg/mL concentration of each drug formulation at 37°C for 1 day. Then the morphological alterations of cell nuclei were distinguished by DAPI staining according to standard instruction.

2.11 Flow cytometry analysis

After the same culture density of target cells in the previous assessment, the cells received PBS (control), free MTX, and MTX-Apt-AuNPs-CS at 100 μg/mL of each drug formulation for 1 day. Afterward, the cells were harvested, cleaned in PBS, trypsinized, and centrifugated at 1,000 rpm for 5 min. The pellets were redispersed in 100 μL of binding buffer and exposed to propidium iodide (PI) and Annexin V-fluorescein isothiocyanate stains in a dark condition for 15 min. The flow cytometry was assessed using a flow cytometer (BD Biosciences, USA).

2.12 Cell cycle assay

First, target cells were exposed to 100 μg/mL PBS, free MTX, and MTX-Apt-AuNPs-CS for 1 day. Next the cells were harvested, rinsed in PBS, and fixed with cold ethanol (70%) overnight. To stain the cells with PI, they were subjected to RNase A (0.1 mg/mL) at 37°C for 30 min in a dark condition. Flow cytometry was employed to measure the percentage of the stained cells in different phases.

2.13 Determination of mitochondrial membrane potential (MMP)

Based on the protocols given by the manufacturer, the target cells were cultured at 5×10^5 cells/well concentration, and 100 μg/mL of each drug formulation was included. After 1 day, 1 mL of culture medium containing JC-1 fluorescence dye (Sigma-Aldrich, USA) was inserted and kept in an incubator for 20 min at 37°C. Ultimately, each dish was rinsed twice with ice-cold JC-1 dye and examined using flow cytometry to identify the MMP.

2.14 Generation of intracellular ROS assay

Herein 2′,7′-Dichlorofluorescein diacetate (DCFH-DA) was employed to stain and measure intracellular reactive oxygen species (ROS). Therefore, the target cells were seeded at a concentration of 1×10^5 cells/well and maintained overnight to confluent. Next 100 μg/mL free drug and drug formulation were added to each cell line and kept for 1 day. Then, PBS containing 10 μM DCFH-DA was included in each sample and kept for 0.5 h at 37°C. Ultimately, a fluorescence microscope (400× magnification) was employed to capture images at 485 nm excitation and 520 nm emission.

2.15 Real-time PCR

After culturing cell lines overnight, they were treated with PBS, free MTX, and MTX-Apt-AuNPs-CS at 100 μg/mL of each drug formulation for 1 day. Next based on the instructions given by the manufacturer, the total RNA was extracted from the cell lines. Similarly, cDNA synthesis and SYBR® Premix Ex Taq TM II kits (TAKARA, Japan) were utilized to convert the RNA to cDNA and perform real-time PCR amplification. β-actin was considered a housekeeping gene (Table 1).

2.16 Western blotting

Like other assessments, after culturing and exposing the cell lines to each nanoformulation for 1 day, cells were gathered, and the total concentration of proteins was estimated by applying Bradford Assay. Next 50 μg protein samples were added, and to separate them, 12% sodium dodecyl sulfate-polyacrylamide gel electrophoresis was carried to the polyvinylidene difluoride membrane. The samples were exposed to 5% bovine serum albumin to block and prepare the membranes for subjecting them to the primers (acquired from Cell Signaling Technology), including B-cell lymphoma-extra large (Bcl-xl), Bax, Bcl-2,

β-actin, cytochrome C (Cyt-C), caspase-3, and caspase-9, at 4°C overnight. At the end of the primary antibody incubation time, the membranes were subjected to the secondary antibody conjugated with horseradish peroxidase for 1 h at room temperature. Chemiluminescence reagent and Image J software were employed to identify and visualize the protein bands. β-actin was considered as an internal control protein.

2.17 *In vivo* study

In this study, 15 4–5 weeks old BALB/c mice (16–20 g) were acquired from the Laboratory Animal Center of Shahid Sadoughi University of Medical Sciences (Yazd, Iran). All animal protocols were conducted under the university's ethics. MDA-MB-231 cells at 4×10^5 concentration were subcutaneously injected into the right flanks of the mice. Once the tumor grew to about 30–40 mm^3, they were categorized into 3 groups of 5. Next testing drugs, including MTX-Apts-CS-AuNPs complex, free MTX with 2.5 mg/kg MTX per mouse, and normal saline, were injected at the tail vein of each category. The tumor size ((length × $width^2$)/2) and body weight were measured every 3 days for 21 days. The fluorescence imaging was conducted using an IVIS imaging system after 4 h of the last injection. All mice were sacrificed on day 21, and their liver, spleen, and kidney were removed and weighed. The organ indexes were calculated by the ratio of the organ weight to the body weight.

2.18 Statistical analysis

Statistical analyses were executed in the SPSS V.18.0 and GraphPad Prism V.8 software. The experimental variables were analyzed using appropriate tests, including one-way ANOVA. All data were stated as mean value ± standard deviation (SD). *P*-value ≤ 0.05 was regarded as statistically significant.

3 Results and discussion

3.1 Characterization of the synthesized MTX-AS1411-CS-AuNPs complex

In various cancer treatment procedures, manifold documents have admitted the evolution of targeted drug delivery to successfully transfer chemo drugs to tumor sites and enhance their therapeutic efficiency on cancerous cells without significant drawbacks on non-cancerous cells [29]. Herein we mainly focused on designing a study to improve the therapeutic efficiency of MTX on breast cancer cells by the construction of the MTX-AS1411-AuNPs-CS complex. As a typical drug delivery vehicle, the size of NPs can enhance the solubility of hydrophobic drugs such as MTX and improve their therapeutic efficacy [30]. The MTX-loaded NPs below 200 nm can successfully circulate in blood vessels and then be preferentially taken up by tumor cells [31]. In the current work, the particle size and morphology of the synthesized CS-AuNPs complex were visualized using the TEM technique, and the images revealed a spherical shape with average sizes of 18.1 ± 1.5 nm (Figure 1a).

Along with nanoparticle size, to characterize the possible changes in functional groups and absorption peaks on the surface of the AuNPs-CS conjugates, an FTIR spectrum was performed. In the FTIR spectra of CS, the functional broadband around 3,402 and 3,292 cm^{-1} was attributed to the N–H or O–H stretching vibrations. The peaks located at 2,856, 1,639, 1,559, 1,382, and 1,074 cm^{-1} were related to the C–H, C═O (amide I), N–H (amid II), C–H, and C–O groups, which were jointed to glucosamine and acetylglucosamine groups of CS (Figure 1b). The characteristic features of the CS spectrum observed in the current study were similar to some prior reports [32]. In the FTIR spectrum of CS-AuNPs, almost identical peaks as that of pure CS were observed, suggesting the presence of CS over AuNPs. The important difference observed in the FTIR of CS-AuNP and pure CS was the shift of a band observed at 1,559 cm^{-1} in the CS spectrum to 1,464 cm^{-1} in the CS-AuNP spectrum, which exhibited

Table 1: The specific primer sequences

Genes	Forward primer	Reverse primer
Bcl-2-associated X protein (Bax)	5′-ACAGAGGGCATGGAGAGAGA-3′	5′-CTGAGAGCAGGGATGTAGCC-3′
B-cell lymphoma 2 (Bcl-2)	5′-CGGCTGAAGTCTCCATTAGC-3′	5′-CCAGGGAAGTTCTGGTGTGT-3′
Caspase 3	5′-CTGTGTGCAGGCTTTTGTGT-3′	5′-CTCAATCACTGCTCGTGGAA-3′
Caspase 9	5′-CGCCACTCTCTCATTCACAA-3′	5′-TCAAGGCAGCCTGTTCTTTT-3′

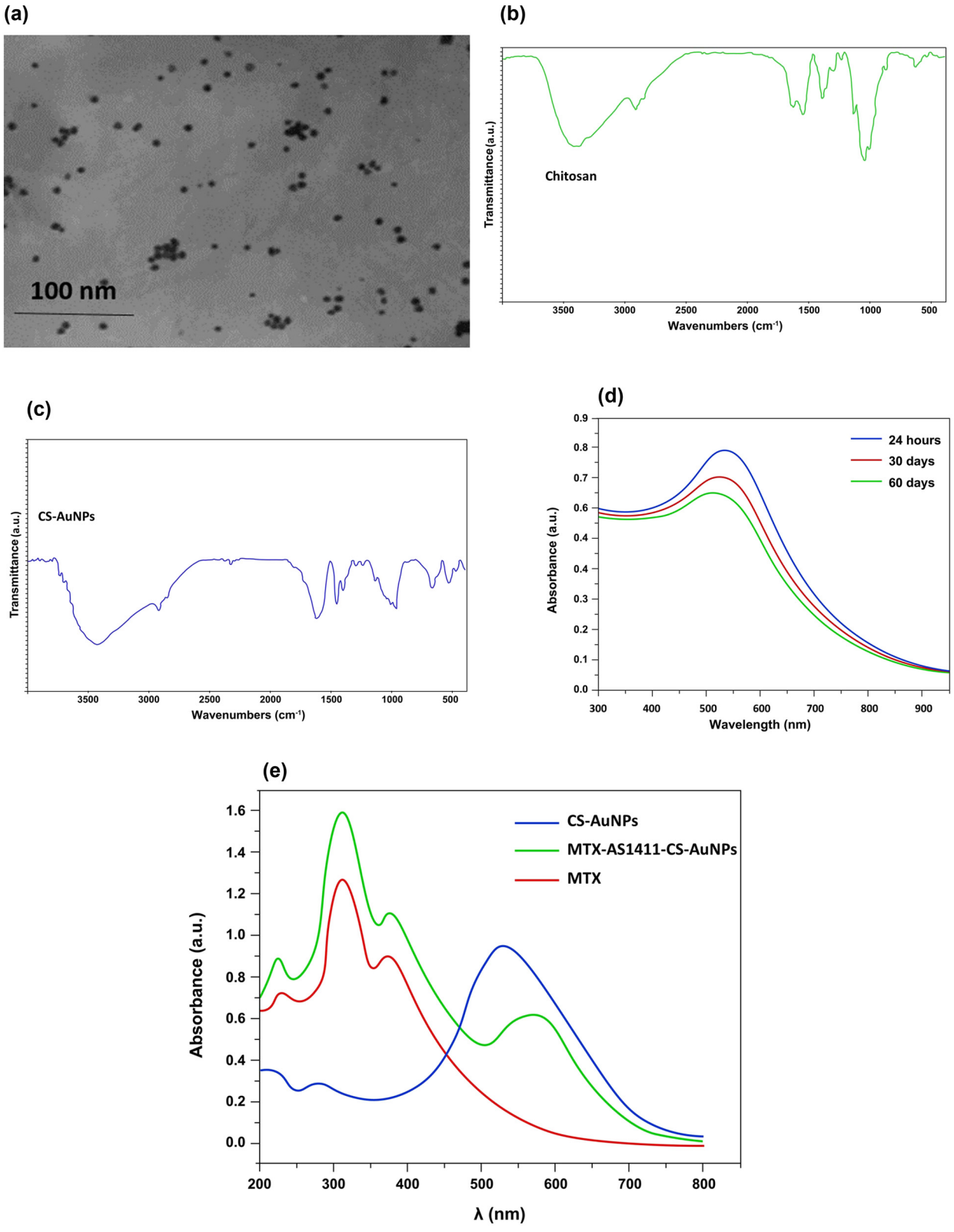

Figure 1: (a) TEM images of CS-AuNPs. (b) FTIR spectra of CS. (c) FTIR spectra of CS-AuNPs. (d) UV-visible absorption spectra of CS-AuNPs at different times. (e) UV-visible absorption spectra of *in vitro* MTX loading onto AS1411-CS-AuNPs.

the attachment of AuNPs to CS through affinity interaction with amino groups, thus reducing the vibration intensity of N–H bond (Figure 1c). Contrary to our expectations, there was no change in the broadband centered around 3,400 cm^{-1}. However, this band's transmittance intensity was diminished compared to the intensity band observed in the FTIR record of CS. The formation of the CS-AuNPs complex could be suggested from the results recorded from FTIR and other experiments. The formation and stability of CS-AuNPs were also checked using UV spectrometer analysis. The surface plasmon resonance (SPR) band was observed approximately at 530 nm and displayed a stable condition after two months (Figure 1d). These properties almost agree with the prior reports [33].

ZP is another essential parameter that predicts both nanosuspension's surface charge and physical stability. The results exhibited that after adding CS to AuNPs, the ZP shifted from −21.6 ± 7.3 to +17.8 ± 4.6 mV due to the presence of the amino groups of CS coating on the AuNPs surface. On the contrary, after loading aptamer, the ZP shifted to −28.6 ± 4.9 mV due to the negatively charged AS1411 on the outer surface of CS-AuNPs, verifying the synthesis of AS1411-CS-AuNPs complex (Table 2). The successful AS1411 absorption was proved by the agarose gel electrophoresis and measuring the absorbance at 260 nm and changes in CS-AuNPs surface charge (Table 2). As shown in Figure S1a, after adding the AS1411 aptamer to the CS-AuNPs complex, its related band did not appear on the agarose gel compared to the bright band of free aptamer, suggesting the successful conjugation of AS1411 and CS-AuNPs complex. On the other hand, the UV absorption spectra of the conjugated AS1411-CS-AuNPs exhibited an absorbance peak at 260 nm, which could suggest successful aptamer attachment on the surface of CS-AuNPs (Figure S1b). Moreover, AS1411 loading efficiency was >85%, confirming AS1411 conjugation to the surface of CS-AuNPs.

We also demonstrated the release of AS1411 from CS-AuNPs in a 10% FBS-containing medium (pH 7.5). Agarose gel electrophoresis illustrated that the AS1411 was slightly released from the nano-vehicle and was detectable after 48 h. These results suggested the protection of AS1411 by the CS-AuNPs at pH 7.4 in FBS solution (Figure S1c).

The stability of NPs in pH 7.4 and pH 5.5 was also determined using DLS analysis. In Figure S2a and S2b, both AuNPs and MTX-AS1411-CS-AuNPs were found to have good stability with minimal size changes at pH 7.4 during 7 days. DLS analysis also revealed that AuNPs and MTX-AS1411-CS-AuNPs (pH 7.4) had a constant surface charge for 7 days (Figure S3a and b). Due to the polycation property of CS, its structure was altered at different pHs. In lower pH solutions, CS molecules become more protonated and extended, and this causes higher hydrodynamic volume NPs [34]. However, the average size of MTX-AS1411-CS-AuNPs became abnormal after 24 h in the pH 5.5 buffer, suggesting the collapses in NPs (Figure S2c).

Table 2: The average size and ZP of AuNPs, CS-AuNPs, AS1411-CS-AuNPs, and MTX-AS1411-CS-AuNPs

Samples	Average size (nm)	ZP (mV)
AuNP	18.1 ± 1.5	−21.6 ± 7.3
CS-AuNP	29 ± 4.2	+17.8 ± 4.6
AS1411-CS-AuNPs	38.9 ± 1.8	−28.6 ± 4.9
MTX-AS1411-CS-AuNPs	62 ± 2.4	−32.1 ± 1.4

Presented data are provided as mean value ± SD (n = 5).

Moreover, the efficiency of MTX loading into Apt-CS-AuNPs conjugates was determined by UV-visible spectroscopy. As presented in Figure 1e, 2 particular absorption bands around 310 and 380 nm corresponded to the absorption of MTX bands, implying that MTX was successfully incorporated into CS-AuNPs. In addition, CS-AuNPs presented a peak around 530 nm, corresponding to the SRP band of spherical AuNPs (Figure 1e). However, the absorbance of MTX-AS1411-CS-AuNP is higher than AuNPs-CS, and the SPR peak shifted to a longer wavelength (580 nm). As the particle diameter increases, the plasmon absorption band shifts toward a longer wavelength (red-shifting) [35].

3.2 *In vitro* release behaviors of MTX from the MTX-AS1411-CS-AuNPs complex

Drug release from NPs at physiological pH plays an important role in forming toxic effects on healthy cells. The slower release of MTX from the vehicle at pH 7.4 was predictable because of the low hydrolysis of amide bonds, which can greatly reduce the systemic toxic effects. Similarly, Luo *et al.* investigated the PEGylated-CS NPs and concluded that the MTX release had a higher pace in acidic pH than physiologic pH, which was similar to our results [36]. The release of MTX from the MTX-AS1411-CS-AuNPs as a drug carrier system was determined at different pHs and times, and the results are shown in Figure 2. To mimic the human healthy and unhealthy physiological environments, the release of MTX-AuNPs-CS-AS1411 was investigated at pH 7.4 and 5.5, respectively. As expected, a higher release rate, 74%, at pH 5.5 (the lysosome pH) than pH 7.4 (the physiological pH) was obtained after 72 h of treatment. Therefore, it was concluded that the release of MTX in acidic pH is highly dependent on the $-NH_2$ groups of CS, which could be selectively protonated in the low pH of

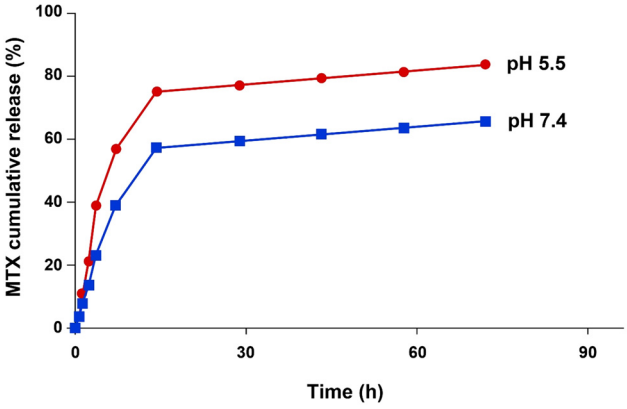

Figure 2: The MTX release profile from the MTX-AS1411-CS-AuNPs conjugate at pH 5.5 (top line) and pH 7.4 (bottom line).

the tumor environment. After penetration into the cells, as the lysosomal compartments have an acidic pH (around 4.5–5.5), it was assumed that MTX was released from the MTX-AuNPs-CS-AS1411, then entered into the cytosol. Moreover, lysosomal organelles contain various hydrolytic enzymes that can break down the internalized AuNPs-CS-AS1411 conjugate [37].

3.3 Cellular internalization of MTX-AuNPs-CS-AS1411 complex

The *in vitro* experimental studies demonstrated that a surface decoration of nano-vesicles with aptamers could cause the enhancement of drug accumulation in targeted tumor sites [38]. For instance, Saravanakumar *et al.* designed aptamer-decorated CS NPs to deliver erlotinib to the A549 cell line. They have declared that the attachment of AS1411 aptamer to the nucleolin of A549 cell at the surface increased when transformed *via* a carrier system and improved the therapeutic efficiency [39]. Herein the specificity of AS1411 toward the cellular trapping of the MTX-CS-AuNPs-AS1411 complex in cancer cells as a cellular model expressing nucleolin protein was investigated. The obtained images of all cell lines displayed the potential of AS1411-functionalized NPs to enter breast cancer cells compared to CHO cells. As shown in Figure 3, MTX-AuNPs-CS-AS1411 complex was successfully taken up by target cells, while less red fluorescence was observed in the CHO cells after treatment with MTX-AuNPs-CS-AS1411 complex. These findings confirmed that the penetration of MTX-AuNPs-CS-AS1411 into the intracellular matrix was higher than free MTX. Also, they indicated that AS1411-decorated AuNPs-CS could assist MTX in entering into the cancer cells (Figure 3).

3.4 *In vitro* cell viability

From the research findings, the utilization of a delivery system for carrying MTX leads to a decrease in the drug's toxic effects in the non-target cells. Zhao *et al.* reported that the cytotoxicity of MTX-loaded NPs against breast cancer cells and tumor tissues was raised appreciably compared to free MTX [40]. Therefore, to explore the *in vitro* efficiency of MTX-AS1411-CS-AuNPs, the cytotoxicity

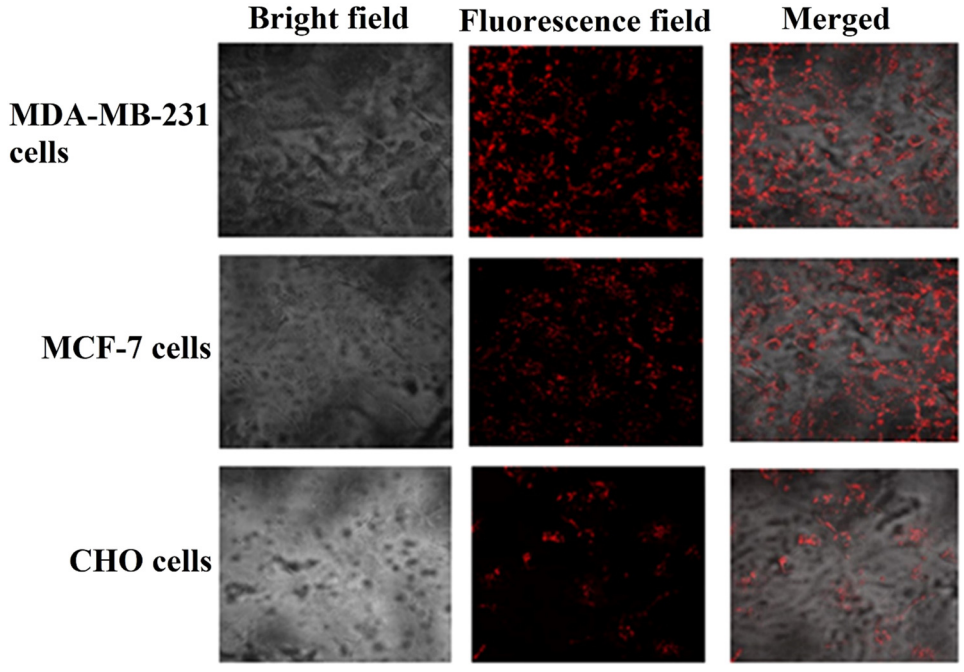

Figure 3: The MTX-AuNPs-CS-AS1411 cellular uptake by the cell lines using confocal fluorescence microscopy.

of free MTX, MTX-CSNPs, and MTX-AS1411-AuNPs-CS was tested on the cell lines using MTT assay. The presented result in Figure 4a revealed that cells treated with CS-AuNPs-AS1411 show no major impact on the viability of cells at all concentrations, which confirmed the biocompatibility of CS-AuNPs-AS1411. Moreover, it was notable that an increase in the concentration of MTX-CS-AuNPs-AS1411 could diminish the survivability of both MDA-MB-231 and MCF-7 cells, but no noteworthy decrease in the viability of normal CHO cells was observed. Thus, it was concluded that the designed MTX-AS1411-AuNPs-CS has no toxic effect on non-target cells (Figure 4b).

3.5 The MMP (ΔΨ*m*)

In this step, the morphological changes in the mitochondrial membranes of the target cells were examined *via* staining the cancer cells with JC-1, a mitochondrial fluorescent dye. The cells were subjected to free MTX and MTX-Apt-AuNPs-CS complex for 24 h. Next the MMP (ΔΨm) disruption was visualized under a fluorescent microscope. Mitochondrial membranes can be detected by the JC-1 and emit red fluorescence light. When the MMP is disrupted, JC-1 cannot aggregate into the mitochondrial membrane and remains monomeric in the cytoplasm that emits green fluorescence. According to fluorescence images, the mean fluorescence intensity changed from red to green in the target cells after exposure to MTX and MTX-Apt-AuNPs-CS for 24 h, representing the Δψm loss due to the depolarization of the mitochondrial membrane. However, the JC-1 dye showed a more intense green fluorescence in the MTX-Apt-AuNPs-CS treatment group than in the free MTX treatment group (Figure 5a).

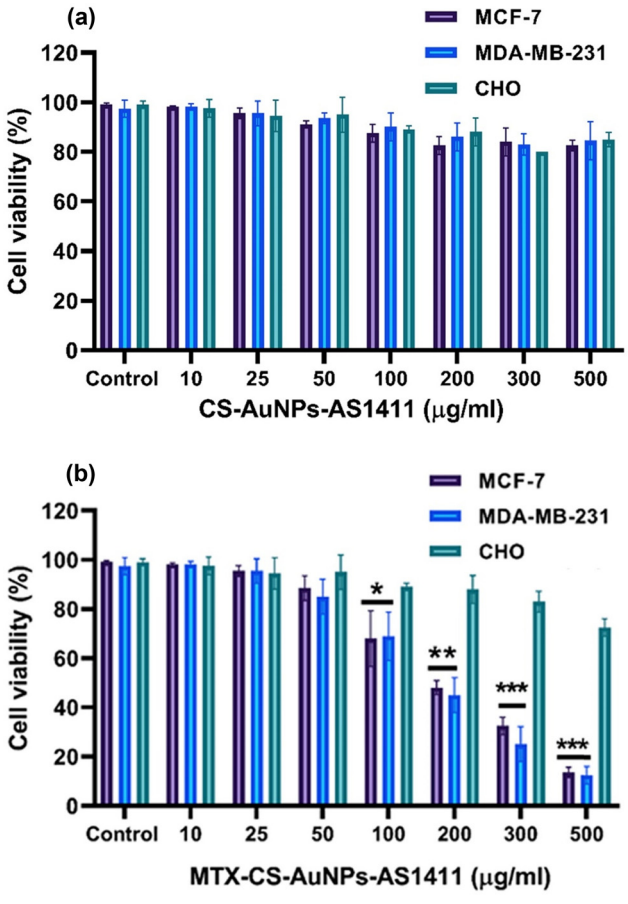

Figure 4: (a) Effect of Apt-AuNPs-CS (without MTX) and (b) MTX-Apt-AuNPs-CS on CHO (non-target), MDA-MB-231 (target), and MCF-7 (target) cell viabilities. The values are stated as mean value ± SD. * $p < 0.05$ shows significant differences.

3.6 ROS generation

The obtained data showed a release of MTX upon entry into the cytoplasm, which caused overproduction of intracellular ROS and induction of oxidative stress situation. As displayed in Figure 5b, the ROS levels were higher in cancer cells treated with MTX-AS1411-AuNPs-CS and free MTX than in untreated cells. The results showed an increased fluorescence intensity in the target cells exposed to MTX-AS1411-AuNPs-CS compared to free MTX, indicating that the MTX delivered by the vehicle was able to generate ROS and induce DNA damage and apoptosis (Figure 5b).

3.7 Apoptosis analysis

Generally, an increase in intracellular ROS levels and the magnitude of damage to DNA and mitochondria confirm the cell's fate proceeding toward the apoptosis pathway. In both the cancer cell lines, the nuclear fragmentation was apperceived by Hoechst and DAPI staining after MTX-CS-AuNPs-AS1411 exposure. The DAPI fluorescent dye forms the dsDNA adducts by which the condensation of apoptotic cell nuclei is detectable. Figure 6a shows that the control group had standard intact nuclei. However, the MTX-treated MDA-MB-231 and MCF-7 cells have abnormal features such as partially fragmented nuclei (Figure 6a). Hence, the number of fragmented cell nuclei were grown after MTX-AS1411-CS-AuNPs uptake by the target cells. Therefore, the MTX-AS1411-CS-AuNPs complex approved its capability of triggering apoptosis. Therefore, to measure the apoptosis rate

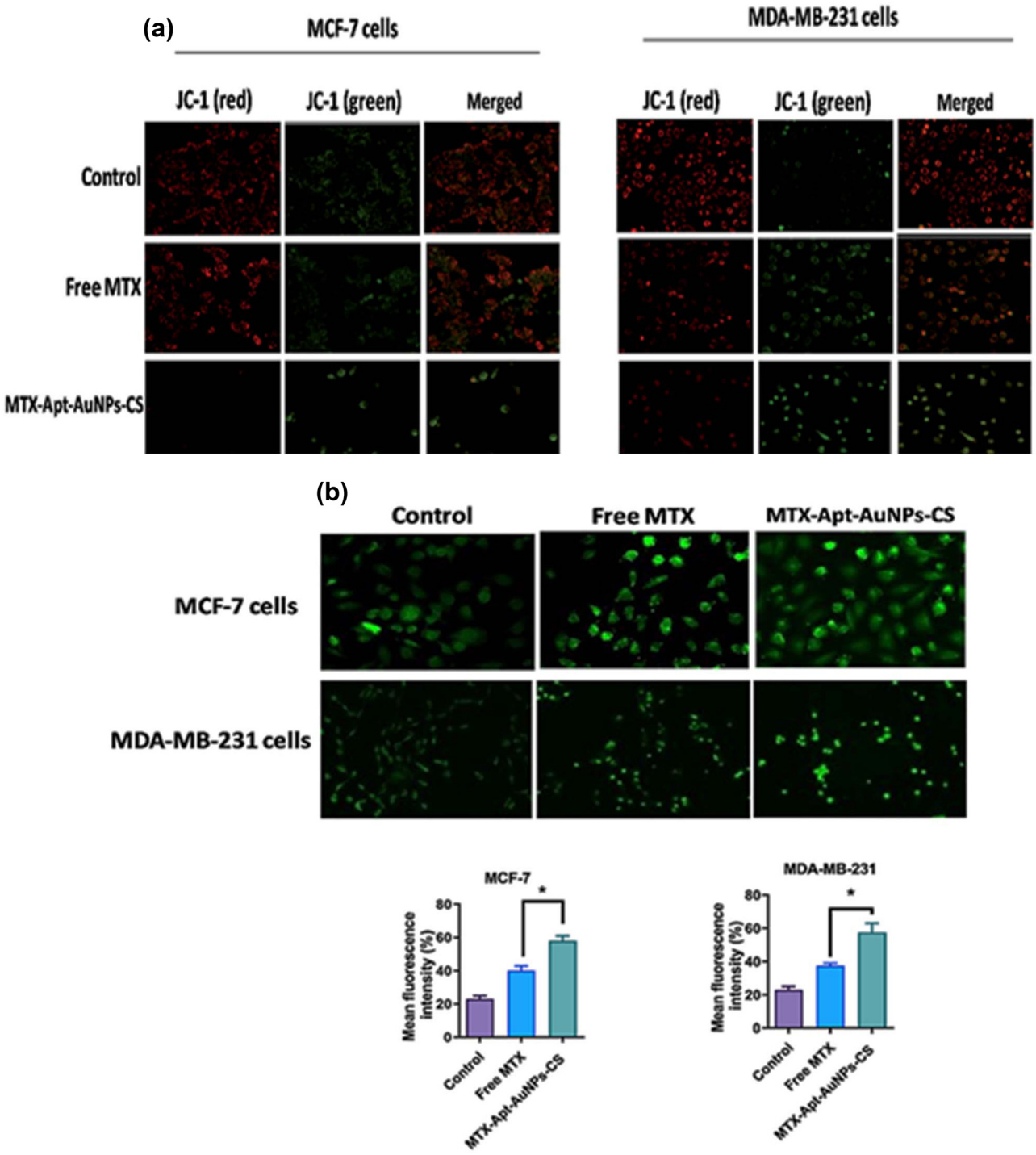

Figure 5: (a) Determination of MMP ($\Delta\Psi m$) disruption by JC-1 dye and (b) ROS using fluorescence microscopy (400× magnification).
* $p < 0.05$ shows significant differences.

of the complex, flow cytometry using annexin V and PI staining methods was used. In Figure 6b, free MTX demonstrated acceptable anti-tumoral activity in the cells at 25 and 28%, respectively. While exposing the cells to functionalized complexes, the death rate rose to 48.5 and 55.5% after incubation for 24 h, respectively. Moreover, after the treatment with the therapeutic drugs, the expression levels of anti-apoptotic and apoptotic markers in the target cells were evaluated using q-RT-PCR and western blotting analyses. The results exhibited that the utilization of the delivery system could

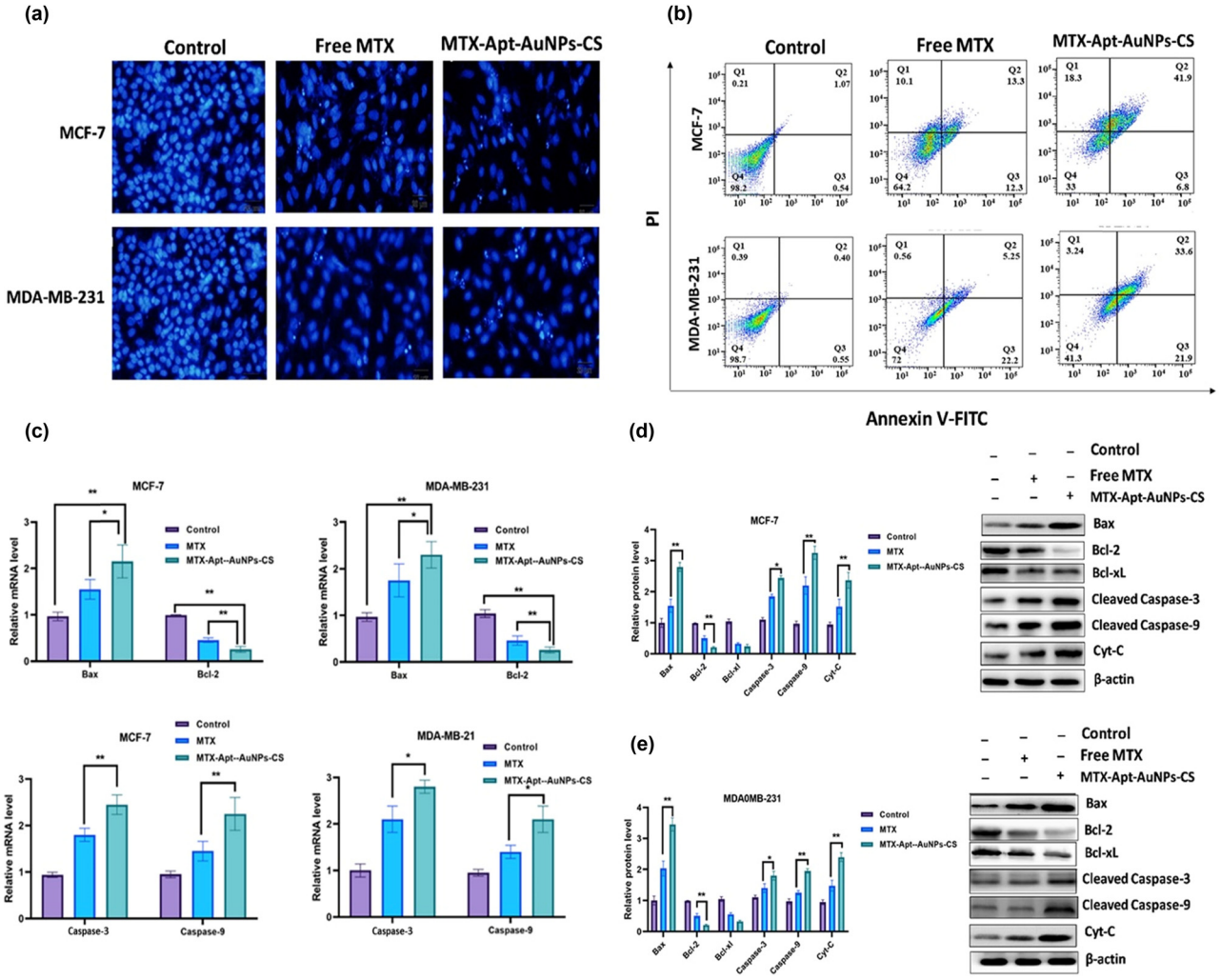

Figure 6: The target cells were incubated with free MTX and MTX-AuNCs-CS-AS1411, and then apoptosis was assessed using (a) DAPI staining by inverted fluorescent microscope and (b) flow cytometry. The apoptosis-related markers were investigated using (c) real-time PCR, and (d, e) western blotting. β-actin was considered as an internal control. * $p < 0.05$ shows significant differences.

downregulate the expression of anti-apoptosis protein (Bcl-2 and Bcl-xL) and upregulate apoptosis-related markers (Cyt-C, Bax, cleaved-caspase-3, and cleaved-caspase-9) compared with MTX alone or control groups (Figure 6c–e).

3.8 Cell cycle analysis

The cell cycle of the target cells was evaluated by being subjected to MTX and MTX-AS1411-CS-AuNPs complex and conducting a flow cytometry and PI staining. Treatment of cells with free MTX showed some alterations in cell cycles in both cell lines, including a reduction in cancer cell percentage in phase S. Interestingly, cell treatment with MTX-AS1411-CS-AuNPs complex increased the cell percentage in sub Go/G1 as a sign of apoptosis (Figure 7). It should be noted that the molecular event of cell cycle arrest is crucial for dealing with the rapid growth of cancer cells. Generally, the cell cycle events are classified into G1, S, and G2 interphases and mitotic (M) stages, which are disturbed under cellular stress [41]. Therefore, a constant high level of MTX-AuNCs-CS-AS1411 complex in the cell lines confirmed the potential of the complex to impel cell cycle arrest to a remarkable extent.

The *in vitro* results were similar to the prior works [42,43]. Mechanistically, MTX could bind to folate receptor and suppress the activity of dihydrofolate reductase, and in turn, impair DNA synthesis, inhibit cell proliferation, and finally induce cell death in the rapidly proliferating cancer cells [11]. Accumulative evidence potentially revealed that the MTX conjugation with the suitable NPs could preserve its attachment to the folate receptor and

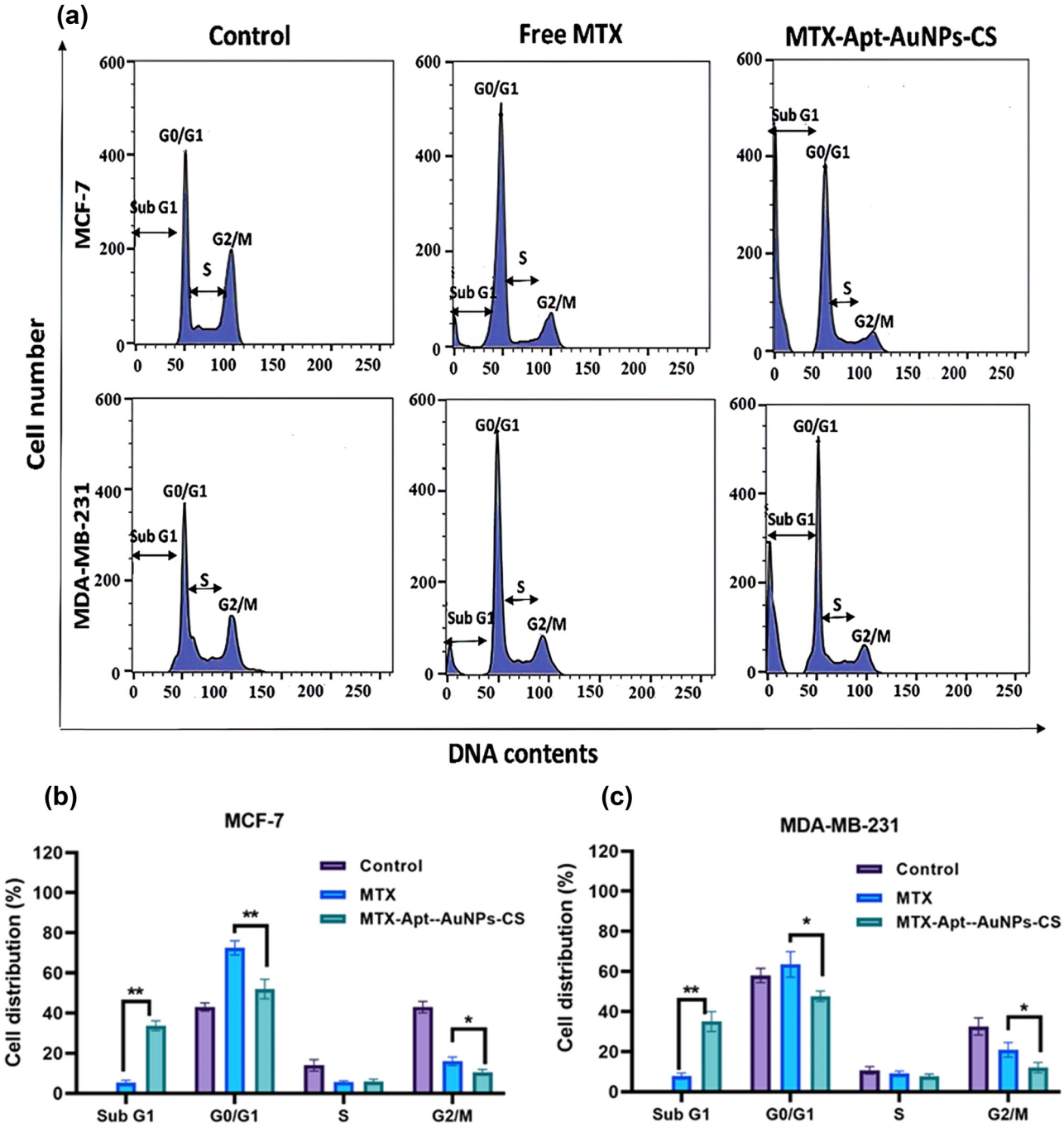

Figure 7: (a) Cell cycle distribution histograms of the target cells. Relative cell cycle distribution of Sub G1, Go/G1, S, and G2 phases in (b) MCF-7 and (c) MDA-MB-231. * $p < 0.05$ shows significant differences.

simultaneously avoid its premature release to decrease the severe toxic effects on healthy tissues during chemotherapy [10]. We have exhibited that the designed nano-system could enhance the drug uptake into the target cells. Our findings indicated that the anti-cancer activity of MTX-AS1411-CS-AuNPs complex against the breast cancer cells was higher than that of the free MTX. MTX released from the vehicle could potentially reduce cell viability in the target cells, disrupt the mitochondrial membrane, cause nuclear fragmentation, and cause subsequent apoptotic cell death and cell cycle arrest. Our results suggested that the MTX-AS1411-CS-AuNPs complex might be a promising drug delivery system, especially for breast carcinoma. The anti-cancer effects of this nano-complex as an *in vivo* system will be investigated.

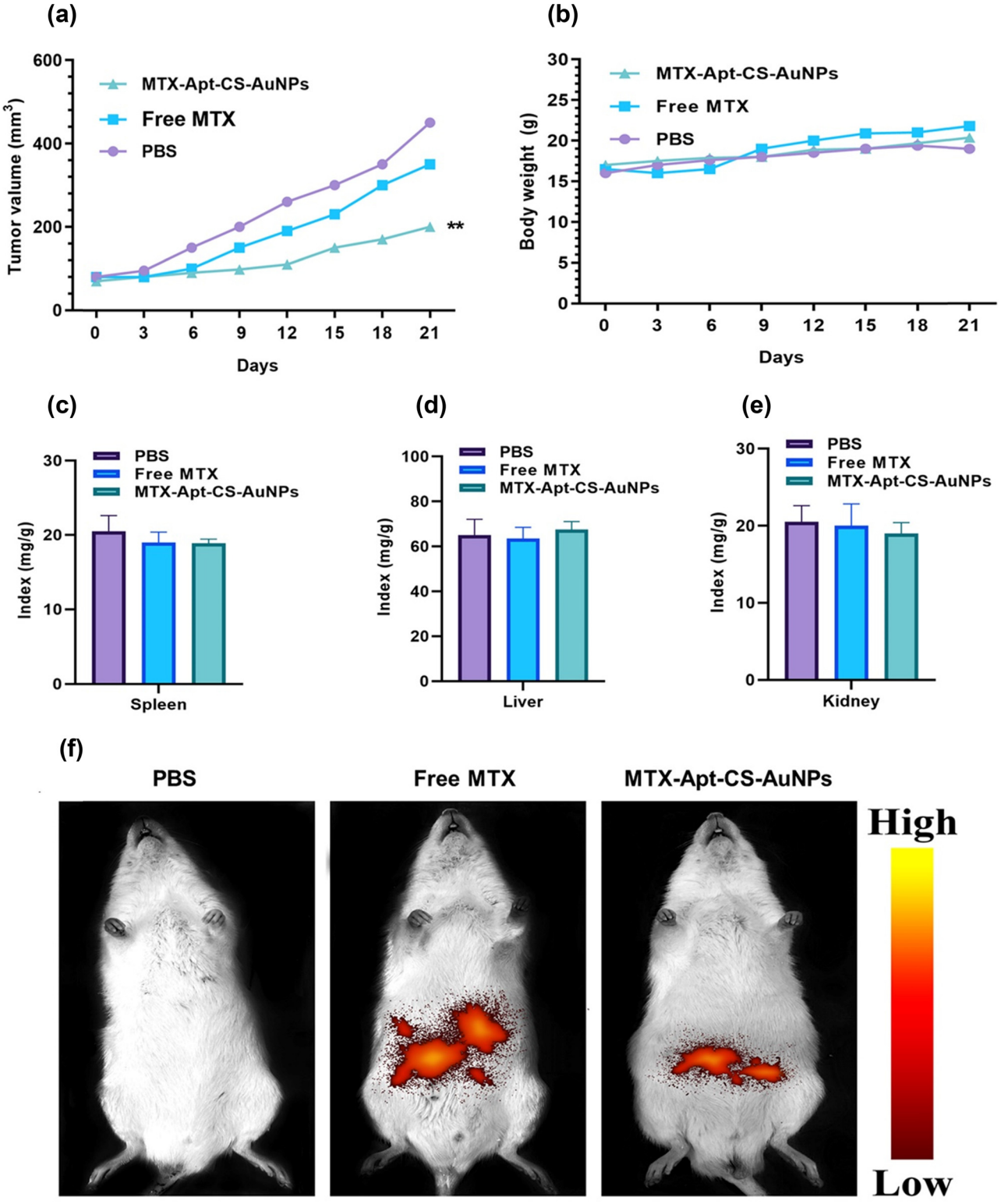

Figure 8: (a) Tumor size, (b) the bodyweight, and (c–e) the organ indexes (liver, spleen, and kidney) of mice after treatment with PBS, free MTX, and MTX-Apt-CS-AuNPs. (f) The fluorescence intensities of mice after 4 h post injection with PBS, free MTX, and MTX-Apt-CS-AuNPs to monitor the targeting effects. $^{**}p < 0.01$ shows significant differences.

3.8.1 *In vivo* study

Tumor-bearing BALB/c mice were employed to investigate the antitumoral activity of MTX in the MTX-AuNCs-CS-AS1411 complex. For this purpose, mice were intravenously subjected to the complex, free MTX, and PBS. As displayed in Figure 8a, the utilization of a delivery system could affect tumor suppression more than those treated with MTX alone or PBS groups ($p < 0.01$). To evaluate the possible side effects, the bodyweight loss and organ indexes were monitored. As reported in Figure 8b, compared to the mice treated with PBS, no considerable alternation in the bodyweight of the mice exposed to MTX-AuNCs-CS-AS1411 was observed. The main organ (liver, spleen, and kidney) tissues were removed and weighed to calculate the organ indexes. The measured ratio were as listed in Figure 8(c–e). Likewise, no considerable alteration was observed between the control and experimental groups in organ indexes.

Moreover, to evaluate the targeting effects of therapeutic drugs, the fluorescence intensities of major organs and tumors were monitored after 4 h of the last injection. The images indicated that the red light was primarily accumulated in the tumor side subjected by the MTX-AuNPs-CS-AS1411 compared to the free MTX. The high entrapment of the complex in cancer sites could be associated with its tumor targeting potential of AS1411 aptamer (Figure 8f).

4 Conclusion

In this experiment, we successfully designed the AuNCs-CS-AS1411 system to deliver MTX to MDA-MB-231 and MCF-7 breast cancer cells and breast tumor site. *In vitro* cellular internalization studies revealed that the designed nano-system could successfully enter into tumor cells, superior to AS1411 as a targeting ligand. Our data showed that MTX released from the vehicle in the target cells could reduce cancer cell viability, disrupt the mitochondrial membrane, cause nuclear fragmentation, and cause subsequent apoptotic cell death and cell cycle arrest. Also, the synthesized nano-system could selectively deliver MTX to the target tumor site and reduce the systematic adverse effect of this chemotherapeutic drug. The results demonstrated a major anti-tumoral activity on the cancer cell lines and minor toxicity on healthy tissues.

Funding information: The authors state no funding involved.

Author contributions: All authors have accepted responsibility for the entire content of this manuscript and approved its submission.

Conflict of interest: The authors state no conflict of interest.

Ethical approval: The research related to animals' use has been complied with all the relevant national regulations and institutional policies for the care and use of animals.

References

[1] Sung H, Ferlay J, Siegel RL, Laversanne M, Soerjomataram I, Jemal A, et al. Global cancer statistics 2020: GLOBOCAN estimates of incidence and mortality worldwide for 36 cancers in 185 countries. CA Cancer J Clin. 2021;71:209–49.

[2] Schirrmacher V. From chemotherapy to biological therapy: A review of novel concepts to reduce the side effects of systemic cancer treatment. Int J Oncol. 2019;54:407–19.

[3] Senapati S, Mahanta AK, Kumar S, Maiti P. Controlled drug delivery vehicles for cancer treatment and their performance. Signal Transduct Target Ther. 2018;3:1–19.

[4] Abtahi NA, Naghib SM, Ghalekohneh SJ, Mohammadpour Z, Nazari H, Mosavi SM, et al. Multifunctional stimuli-responsive niosomal nanoparticles for co-delivery and co-administration of gene and bioactive compound: *In vitro* and *in vivo* studies. Chem Eng J. 2022;429:132090. doi: 10.1016/j.cej.2021.132090.

[5] Mazidi Z, Javanmardi S, Naghib SM, Mohammadpour Z. Smart stimuli-responsive implantable drug delivery systems for programmed and on-demand cancer treatment: An overview on the emerging materials. Chem Eng J. 2022;433:134569. doi: 10.1016/j.cej.2022.134569.

[6] Yaghoubi F, Naghib SM, Motlagh NSH, Haghiralsadat F, Jaliani HZ, Tofighi D, et al. Multiresponsive carboxylated graphene oxide-grafted aptamer as a multifunctional nanocarrier for targeted delivery of chemotherapeutics and bioactive compounds in cancer therapy. Nanotechnol Rev. 2021;10:1838–52. doi: 10.1515/ntrev-2021-0110.

[7] Abtahi NA, Naghib SM, Haghiralsadat F, Reza JZ, Hakimian F, Yazdian F, et al. Smart stimuli-responsive biofunctionalized niosomal nanocarriers for programmed release of bioactive compounds into cancer cells *in vitro* and *in vivo*. Nanotechnol Rev. 2021;10:1895–911. doi: 10.1515/ntrev-2021-0119.

[8] Rahimzadeh Z, Naghib SM, Askari E, Molaabasi F, Sadr A, Zare Y, et al. A rapid nanobiosensing platform based on herceptin-conjugated graphene for ultrasensitive detection of circulating tumor cells in early breast cancer. Nanotechnol Rev. 2021;10:744–53. doi: 10.1515/ntrev-2021-0049.

[9] Shakeran Z, Keyhanfar M, Varshosaz J, Sutherland DS. Biodegradable nanocarriers based on chitosan-modified mesoporous silica nanoparticles for delivery of methotrexate for application in breast cancer treatment. Mater Sci Eng C. 2021;118:111526.

[10] Fathi M, Barar J, Erfan-Niya H, Omidi Y. Methotrexate-conjugated chitosan-grafted pH-and thermo-responsive magnetic nanoparticles for targeted therapy of ovarian cancer. Int J Biol Macromol. 2020;154:1175–84.
[11] Panji M, Behmard V, Zare Z, Malekpour M, Nejadbiglari H, Yavari S, et al. Synergistic effects of green tea extract and paclitaxel in the induction of mitochondrial apoptosis in ovarian cancer cell lines. Gene. 2021;787:145638.
[12] Johari-Ahar M, Barar J, Alizadeh AM, Davaran S, Omidi Y, Rashidi M-R. Methotrexate-conjugated quantum dots: synthesis, characterisation and cytotoxicity in drug resistant cancer cells. J Drug Target. 2016;24:120–33.
[13] Amina SJ, Guo B. A review on the synthesis and functionalization of gold nanoparticles as a drug delivery vehicle. Int J Nanomed. 2020;15:9823.
[14] Park SJ. Protein–nanoparticle interaction: corona formation and conformational changes in proteins on nanoparticles. Int J Nanomed. 2020;15:5783.
[15] Mohammed MA, Syeda J, Wasan KM, Wasan EK. An overview of chitosan nanoparticles and its application in non-parenteral drug delivery. Pharmaceutics. 2017;9:53.
[16] Gooneh-Farahani S, Naghib SM, Naimi-Jamal MR, Seyfoori A. A pH-sensitive nanocarrier based on BSA-stabilized graphene-chitosan nanocomposite for sustained and prolonged release of anticancer agents. Sci Rep. 2021;11:17404. doi: 10.1038/s41598-021-97081-1.
[17] Gooneh-Farahani S, Naghib SM, Naimi-Jamal MR. A novel and inexpensive method based on modified ionic gelation for pH-responsive controlled drug release of homogeneously distributed chitosan nanoparticles with a high encapsulation efficiency. Fibers Polym. 2020;21:1917–26. doi: 10.1007/s12221-020-1095-y.
[18] Wang W, Meng Q, Li Q, Liu J, Zhou M, Jin Z, et al. Chitosan derivatives and their application in biomedicine. Int J Mol Sci. 2020;21:487.
[19] Jhaveri J, Raichura Z, Khan T, Momin M, Omri A. Chitosan nanoparticles-insight into properties, functionalization and applications in drug delivery and theranostics. Molecules. 2021;26:272.
[20] Briolay T, Petithomme T, Fouet M, Nguyen-Pham N, Blanquart C, Boisgerault N. Delivery of cancer therapies by synthetic and bio-inspired nanovectors. Mol Cancer. 2021;20:1–24.
[21] Zhang Y, Lai BS, Juhas M. Recent advances in aptamer discovery and applications. Molecules. 2019;24:941.
[22] Shahidi M, Abazari O, Bakhshi A, Zavarreza J, Modarresi M, Haghiralsadat F, et al. Multicomponent siRNA/miRNA-loaded modified mesoporous silica nanoparticles targeted bladder cancer for a highly effective combination therapy. Front Bioeng Biotechnol. 2022;10:949704. doi: 10.3389/fbioe.2022.949704.
[23] Panji M, Behmard V, Zare Z, Malekpour M, Nejadbiglari H, Yavari S, et al. Suppressing effects of Green tea extract and Epigallocatechin-3-gallate (EGCG) on TGF-β-induced Epithelial-to-mesenchymal transition via ROS/Smad signaling in human cervical cancer cells. Gene. 2021;794:145774.
[24] Mu W, Chu Q, Liu Y, Zhang N. A review on nano-based drug delivery system for cancer chemoimmunotherapy. Nano-Micro Lett. 2020;12:1–24.
[25] Franconetti A, Carnerero JM, Prado-Gotor R, Cabrera-Escribano F, Jaime C. Chitosan as a capping agent: Insights on the stabilization of gold nanoparticles. Carbohydr Polym. 2019;207:806–14.
[26] Lai C, Liu X, Qin L, Zhang C, Zeng G, Huang D, et al. Chitosan-wrapped gold nanoparticles for hydrogen-bonding recognition and colorimetric determination of the antibiotic kanamycin. Microchim Acta. 2017;184:2097–105.
[27] Kukreti S, Kaushik M. Exploring the DNA damaging potential of chitosan and citrate-reduced gold nanoparticles: physico-chemical approach. Int J Biol Macromol. 2018;115:801–10.
[28] Vandghanooni S, Eskandani M, Barar J, Omidi Y. AS1411 aptamer-decorated cisplatin-loaded poly (lactic-co-glycolic acid) nanoparticles for targeted therapy of miR-21-inhibited ovarian cancer cells. Nanomedicine. 2018;13:2729–58.
[29] Patra JK, Das G, Fraceto LF, Campos EVR, del Pilar Rodriguez-Torres M, Acosta-Torres LS, et al. Nano based drug delivery systems: recent developments and future prospects. J Nanobiotechnol. 2018;16:1–33.
[30] Gaumet M, Vargas A, Gurny R, Delie F. Nanoparticles for drug delivery: the need for precision in reporting particle size parameters. Eur J Pharm Biopharm. 2008;69:1–9.
[31] Prabha S, Arya G, Chandra R, Ahmed B, Nimesh S. Effect of size on biological properties of nanoparticles employed in gene delivery. Artif Cells Nanomed Biotechnol. 2016;44:83–91.
[32] Mohan CO, Gunasekaran S, Ravishankar CN. Chitosan-capped gold nanoparticles for indicating temperature abuse in frozen stored products. Npj Sci Food. 2019;3:1–6.
[33] Tyagi H, Kushwaha A, Kumar A, Aslam M. A facile pH controlled citrate-based reduction method for gold nanoparticle synthesis at room temperature. Nanoscale Res Lett. 2016;11:1–11.
[34] Tsai M-L, Chen R-H, Bai S-W, Chen W-Y. The storage stability of chitosan/tripolyphosphate nanoparticles in a phosphate buffer. Carbohydr Polym. 2011;84:756–61.
[35] Saleh NM, Aziz AA. Simulation of surface plasmon resonance on different size of a single gold nanoparticle. Journal of Physics: Conference Series, vol. 1083, IOP Publishing; 2018, p. 12041.
[36] Luo F, Li Y, Jia M, Cui F, Wu H, Yu F, et al. Validation of a Janus role of methotrexate-based PEGylated chitosan nanoparticles *in vitro*. Nanoscale Res Lett. 2014;9:1–13.
[37] Rosenholm JM, Peuhu E, Bate-Eya LT, Eriksson JE, Sahlgren C, Lindén M. Cancer-cell-specific induction of apoptosis using mesoporous silica nanoparticles as drug-delivery vectors. Small. 2010;6:1234–41.
[38] Zhu G, Chen X. Aptamer-based targeted therapy. Adv Drug Deliv Rev. 2018;134:65–78.
[39] Saravanakumar K, Sathiyaseelan A, Mariadoss AVA, Jeevithan E, Hu X, Shin S, et al. Dual stimuli-responsive release of aptamer AS1411 decorated erlotinib loaded chitosan nanoparticles for non-small-cell lung carcinoma therapy. Carbohydr Polym. 2020;245:116407.
[40] Zhao Y, Guo Y, Li R, Wang T, Han M, Zhu C, et al. Methotrexate nanoparticles prepared with codendrimer from polyamidoamine (PAMAM) and oligoethylene glycols (OEG) dendrons: Antitumor efficacy *in vitro* and *in vivo*. Sci Rep. 2016;6:1–11.
[41] Goel S, DeCristo MJ, McAllister SS, Zhao JJ. CDK4/6 inhibition in cancer: beyond cell cycle arrest. Trends Cell Biol. 2018;28:911–25.

[42] Ciro Y, Rojas J, Di Virgilio AL, Alhajj MJ, Carabali GA, Salamanca CH. Production, physicochemical characterization, and anticancer activity of methotrexate-loaded phytic acid-chitosan nanoparticles on HT-29 human colon adenocarcinoma cells. Carbohydr Polym. 2020;243:116436.

[43] Akbari E, Mousazadeh H, Sabet Z, Fattahi T, Dehnad A, Akbarzadeh A, et al. Dual drug delivery of trapoxin A and methotrexate from biocompatible PLGA-PEG polymeric nanoparticles enhanced antitumor activity in breast cancer cell line. J Drug Deliv Sci Technol. 2021;61:102294.